ACS OMEGA

http://pubs.acs.org/journal/acsodf

Article

Hierarchical Tantalum Oxide Composite for Efficient Solar-Driven Water Purification

Xuanbo Chen,* Yingqi Zhu, Shuyong Liu,* Jinlin Liu, and Jing Li

Cite This: *ACS Omega* 2023, 8, 29025−29032

Read Online

ACCESS | Metrics & More | Article Recommendations | Supporting Information

ABSTRACT: Applying solar energy to generate drinking water is a clean and low-energy exhaust route to address the issue of water purification. The current challenge with solar vapor generation is constructing nano/micro-hierarchical structures that can convert solar irradiation into exploitable thermal energy with high efficiency. Although various structures and material designs have been reported in recent years, solar vapor conversion can be improved by integrating light harvesting, thermal concentration, and water diffusion. Because of the optimized solar harvesting, enhanced heat capacity, and specified diffusive path endowed by the hierarchical composite structure, amorphous tantalum oxide/carbon-based yolk−shell structures (α-Ta_2O_5/C YS) for highly efficient solar vapor generation under 1 sun illumination are applied in this study. As a result, the α-Ta_2O_5/C YS realized a water evaporation rate of 3.54 kg m^{-2} h^{-1} with a solar-thermal conversion efficiency of 91% under one sun irradiation (1 kW m^{-2}) with excellent evaporation stability. The collected water from seawater meets the World Health Organization drinking water standard. Importantly, reactive oxygen species enabled by α-Ta_2O_5 could be produced for water sterilization, exhibiting a facile way for application in various scenarios to acquire drinkable water.

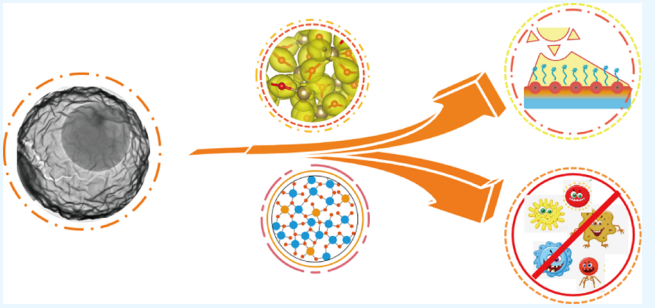

INTRODUCTION

Providing inexpensive drinking water is an increasingly serious challenge due to the various byproducts of industrial manufacture. Public health is threatened by a wide variety of water pollutants, including bacteria and viruses. Because of the widespread and ready availability of seawater, there is a huge demand for the desalination of seawater for acquiring freshwater. Furthermore, drinking water obtained from harsh environments, such as isolated reefs and border posts, is critical for defense supply in regions with no electricity. However, water treatment generally requires the removal of multiple pollutants; basic treatment often relies on aggregation/precipitation or media filtration of colloidal and other suspended matter, which cannot provide sterilization and inactivation. Recently, solar-driven interfacial water evaporation has attracted tremendous research attention because of the high water purification capacity and the wide range of applications,[1,2] as well as high solar conversion efficiency and convertible industrial potential.[3,4]

A critical aspect of efficient solar evaporation is designing optimized interfacial evaporation materials. Numerous studies have been focused on this issue. The composition of solar-driven interfacial materials mainly includes carbon materials,[5,6] metal-based plasmonic materials,[7−9] ceramic composites,[10] and polymer hydrogel materials.[11−13] Precious-metal-based solar vapor materials have attracted attention due to their strong plasma resonance absorption and superior heat-transfer properties;[14] while evaporating actual water, metal-based materials display an excellent antibacterial behavior against *Escherichia coli* and *Staphylococcus aureus*,[15] but it is unlikely to achieve large-scale mass production. Polymer hydrogel is a material with the highest evaporation rate in reported research.[16] Its three-dimensional interconnected porous structure and abundant hydrophilic functional groups on the surface are important bridges for efficient water diffusion[17] and have application potential in organic compound enrichment and extraction.[18] Unfortunately, polymer hydrogels suffer from unstable synthesis and easy aging. Semiconductor solar vapor materials possess a large number of free carriers,[19] strong localized surface plasmon resonance (LSPR) effect,[20,21] significant thermal concentration effect,[22−24] and easily controlled nanostructures, especially some metal oxides, such as magnetic Fe_3O_4, which can facilitate the recovery and reuse of suspended particles.[25] Carbon-based solar vapor materials possess a wide light absorption range, hydrophilicity/hydrophobicity shift, and micropores/mesopores. Biomass carbon materials have a low cost and a penetrating hierarchical pore structure, which is conducive to water diffusion and trans-

Received: March 21, 2023
Accepted: July 21, 2023
Published: August 4, 2023

https://doi.org/10.1021/acsomega.3c01858
ACS Omega 2023, 8, 29025−29032

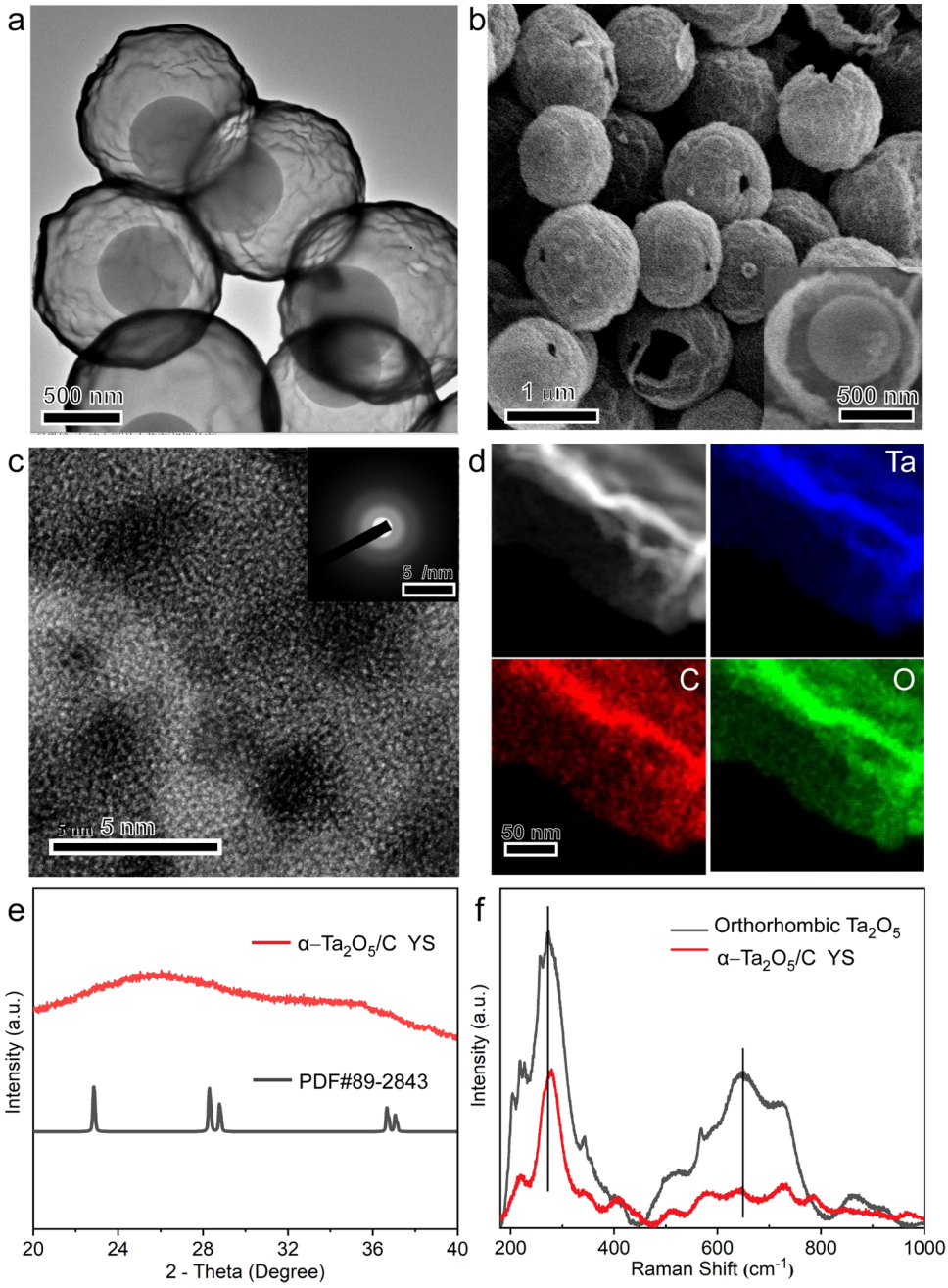

Figure 1. Morphology and structure of α-Ta_2O_5/C YS. (a) TEM image of α-Ta_2O_5/C YS; (b) SEM image of α-Ta_2O_5/C YS (inset: the broken structure); (c) HAADF-TEM and SAED pattern (Inset) of α-Ta_2O_5/C YS; (d) EELS mapping images of the shell for the broken structure; (e) XRD pattern and (f) Raman spectra of α-Ta_2O_5/C YS.

mission.[26−28] Solar vapor composites are composed of various materials mentioned above, and the preparation process is often relatively complicated, making mass-scale production difficult.[29−31]

Semiconductors as good candidates for solar-thermal interfacial materials may be irreplaceable for such varied applications. One reason is that semiconductor materials would generate reactive oxygen species (ROS, such as hydroxyl radicals, superoxides, and singlet oxygen), which are used for rapid sterilization via photocatalytic oxidation. Another reason is that semiconductors with highly adjustable light harvesting, intrinsic enhanced thermalization, and excellent stability can be simultaneously realized.

Currently, oxygen defects have been introduced into semiconductors (metal oxides, such as TiO_{2-x},[32] MoO_{3-x},[33] and WO_{3-x}[34]), which could efficiently narrow the band gap and enhance the light absorption. However, these oxygen-deficient nonstoichiometric metal oxides become relatively unstable under harsh environments. For this reason, the introduction of heteroatoms, such as C or N, can not only resolve the instability caused by oxygen defects but also facilitate water diffusion by reducing the interaction force[35] and improving the surface area.[36]

Generally, ideal solar evaporation materials must meet the following criteria: (i) they usually have a wide absorption capability, including a nanostructure design with higher light harvesting;[37] (ii) they must exhibit less emission, which

https://doi.org/10.1021/acsomega.3c01858
ACS Omega 2023, 8, 29025−29032

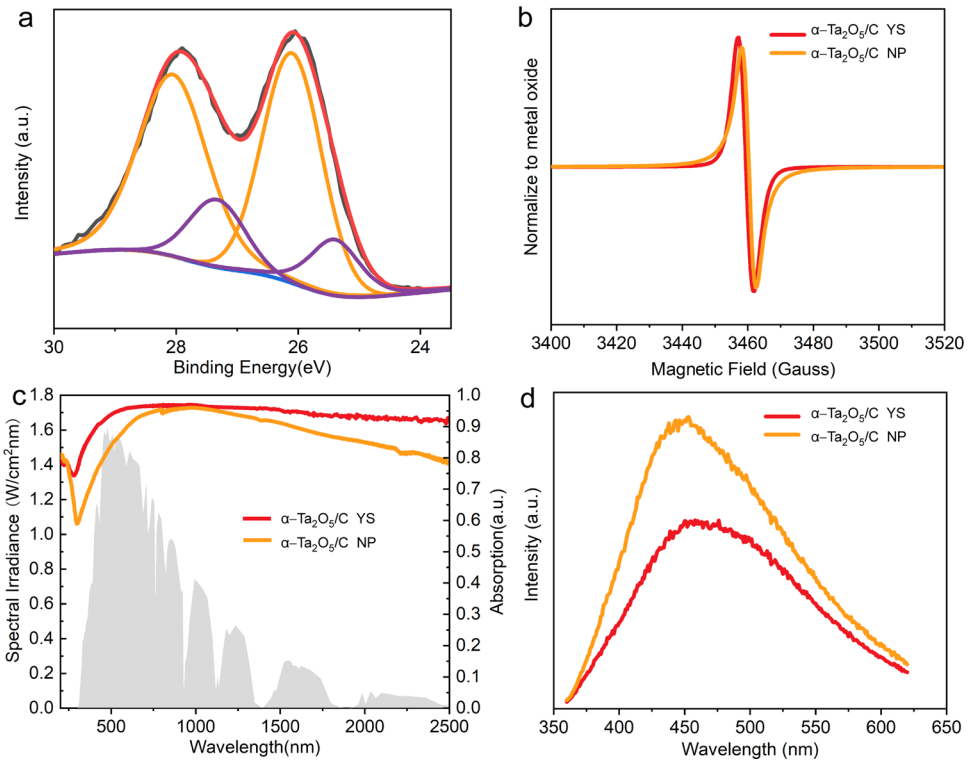

Figure 2. Solar absorbance and solar conversion of α-Ta_2O_5/C YS and α-Ta_2O_5/C NP. (a) XPS spectra of α-Ta_2O_5/C YS; (b) EPR spectra and (c) UV−vis−NIR spectra of the YS and NP samples; and (d) photoluminescence (PL) spectra of the as-prepared sample; the excitation wavelength is 350 nm.

ensures a higher solar-heat conversion efficiency;[38] and (iii) they must have corrosion resistance and excellent stability in harsh environments and in the presence of water.[39] Therefore, excellent physicochemical stability against corrosion by acidic and alkaline water, as well as the thermal concentration endowed by an indirect bandgap structure and high diffusive activation energy of the Ta atom, are desirable.[40] Therefore, Ta_2O_5 is a potential candidate for applications in thermal and environmental barrier coatings.[41] Notably, Ta_2O_5 with a large band gap produces a large amount of reactive oxygen species (ROS) for ultrafast sterilization and virus removal from water bodies. By introducing C heteroatoms, the light-harvesting efficiency and surface energy of Ta_2O_5 can be optimized. Inspired by these advantages, we applied Ta_2O_5 and C compounds as solar evaporation materials in this work.

In addition, the nano-microstructures of tantalum oxides were mainly synthesized as low-dimensional nanoparticles or fibers, inducing suboptimal water diffusion. As a result, the rational design of these solar vapor generation materials with three-dimensional (3D) microscale structures remains challenging. A specific micro-nano structural model, Yolk-shell structure derived from hollow multishelled spheres, with internal cores separated by external shells, reserving specific dimensional voids, have been confirmed to to benefit light harvesting[42,43] and mass diffusion.[44,45] Thermal concentration endowed by this hierarchical porous structure would also enhance the solar-thermal conversion efficiency.[46,47]

In this work, α-Ta_2O_5/C yolk−shell (α-Ta_2O_5/C YS) with a sub-micrometer structure was successfully synthesized by using a hydrothermal calcination process.[48−52] Because of the disordered atomic arrangement and unique hierarchical hollow structures, the amorphous Ta_2O_5/C YS exhibited a higher heat concentration and enhanced capillary diffusion properties, with the highest evaporation rate of up to 3.54 kg m^{-2} h^{-1} and 91% solar-heat conversion efficiency. Furthermore, it maintained good stability for up to 15 days without a decrease in activity.

RESULTS AND DISCUSSION

α-Ta_2O_5/C YS was prepared through one-step cation adsorption and lower temperature calcination based on carbon microsphere (CMS) templates. The precious structure can be controlled by adjusting the concentration of the metal ions and heating conditions. Because of the adsorption solvent with lower surface tension, absolute ethanol was substituted with acetone to improve the cation diffusion depth and adsorption capacity. Furthermore, the heating atmosphere and temperature were confirmed to adjust the burning rate, which can suitably control the composition and yolk-like diameter of this specific structure. The transmission electron microscopy (TEM) and scanning electron microscopy (SEM) images in Figure 1a,b display Ta_2O_5/C YS, which has a relatively uniform diameter and a concave−convex surface, and the broken structure indicates that the solid microsphere and shell are separated by the large cavity (inset in Figure 1b). Notably, Ta_2O_5/C YS with a short-range ordered amorphous phase (α-Ta_2O_5/C) was fabricated at 300 °C for 90 min, which is proven by high-angle annular dark-field transmission electron microscopy (HAADF-TEM) showing the random arrangement of atoms in shells (Figure 1c). Selected area electron diffraction (SAED) shows the dispersion ring in the prepared sample, which also confirms the disordered amorphous structure (inset in Figure 1c). Interestingly, electron energy loss spectroscopy (EELS) mapping revealed that the shell of this sample is composed of Ta, O, and C atoms (Figure 1d).

https://doi.org/10.1021/acsomega.3c01858
ACS Omega 2023, 8, 29025−29032

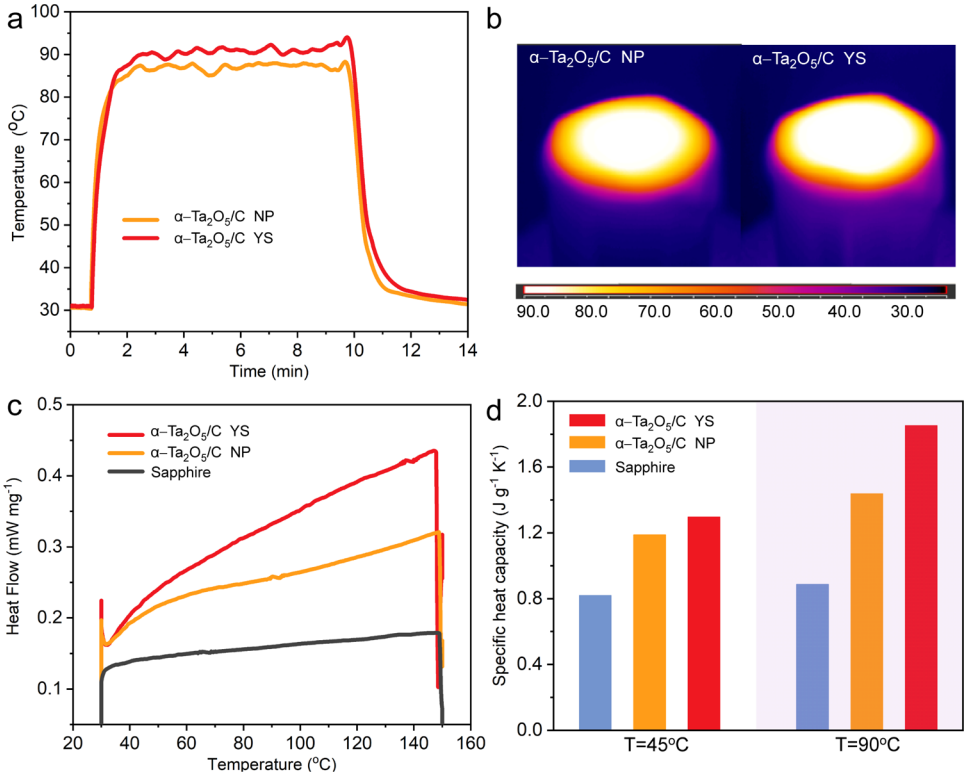

Figure 3. Solar-thermal conversion of α-Ta_2O_5/C YS and α-Ta_2O_5/C NP. (a) Temperature-changing course of different samples under solar illumination of 1 kW m^{-2}. (b) Infrared image of α-Ta_2O_5/C yolk–shell and α-Ta_2O_5/C nanoparticles under solar illumination of 1 kW m^{-2} for 60 min. (c) Heat capacity of materials with different morphologies measured by the sapphire reference method. (d) Specific heat capacity of different samples compared with the sapphire reference at 45 and 90 °C.

The morphology and carbon amount of this structure could be controlled by a specific annealing procedure (Tables S1 and S2).

Similarly, the X-ray diffraction (XRD) results show no diffraction peak assigned to Ta_2O_5/C YS, based on the low-temperature phase Ta_2O_5 (orthorhombic: PDF number 89-2843, Figure 1e), which confirms that a long-range disordered structure exists in tantalum oxide/carbon composites. As observed in the Raman spectra, the Raman bands between 100 and 450 cm^{-1} are associated with O–Ta–O bending modes in TaO_6 octahedra,[53] Raman peaks of the samples prepared by us have a blue shift, compared with orthorhombic Ta_2O_5, and their intensities weaken to a half, which indicates that the TaO_6 unit is retained in the prepared composites (Figure 1f). However, the peaks between 450 and 900 cm^{-1} mainly correspond to the various Ta–O stretching modes associated with edge-shared polyhedra. The disordered results in these Raman bands from the sample indicate that it has a long-range disordered atomic arrangement. All of these features are in good agreement with the XRD results.

Surface valence state analysis was conducted by X-ray photoelectron spectroscopy (XPS), as shown in Figures 2a and S1. The Ta^{5+} $4f_{7/2}$ peak located at 25.9 eV in the XPS spectrum[54] of α-Ta_2O_5/C YS confirmed that the majority of the Ta element is in the Ta^{5+} state, while a large quantity of C atoms are dispersed around the TaO_6 unit or interval positions; C atoms have a lower electronegativity compared with O atoms, which results in a differential charge density around the Ta atoms as well as dangling bonds at the amorphous surface. Thus, a tiny valence deviation exists in the prepared samples. Electron paramagnetic resonance (EPR) spectra verified that the unpaired electrons are caused by C heteroatoms and oxygen defects. The indicator values of the g peak at 2.015 and 2.002 correspond to oxygen vacancies and C heteroatoms,[55] respectively (Figure 2b). The light-harvesting capacity of the prepared samples should be interrelated to these unpaired electrons.

To experimentally assess the light-harvesting capacity, we further measured the ultraviolet–visible–near infrared (UV–vis–NIR) spectra with different morphological structures (the yolk–shell samples synthesized by us and nanoparticles). For comparison, α-Ta_2O_5/C nanoparticles (NPs) were synthesized through a hydrothermal process by a similar heating procedure (Figures S2–S4). The total absorption capacity of the α-Ta_2O_5/C YS sample is 92.1%, which is higher than that of α-Ta_2O_5/C NP (86.5%). Density functional theory (DFT) calculations show that α-Ta_2O_5/C has an indirect band gap of 0.12 eV (Figure S5), sharply decreasing the band gap of Ta_2O_5.[46] Moreover, the PL spectra confirm that α-Ta_2O_5/C YS has a lower PL intensity (Figure 2d) compared with α-Ta_2O_5/C NP. This indicates that the yolk–shell sample can not only harvest more light but also transfer more photoexcited electrons to nonradiative relaxation, i.e., solar-thermal conversion.

As a result, the surface temperature of amorphous Ta_2O_5/C YS increased from 30 °C to 91 °C in 3 min under solar illumination of 1 kW m^{-2} (Figure 3a,b), which is higher than that of α-Ta_2O_5/C NPs (86 °C). With the same weight compared with α-Ta_2O_5/C NPs, the α-Ta_2O_5/C YS powder has a larger luminal volume because of the hierarchical cavity structure, which may be responsible for the unique heat concentration. The heat capacity of α-Ta_2O_5/C was exper-

https://doi.org/10.1021/acsomega.3c01858
ACS Omega 2023, 8, 29025–29032

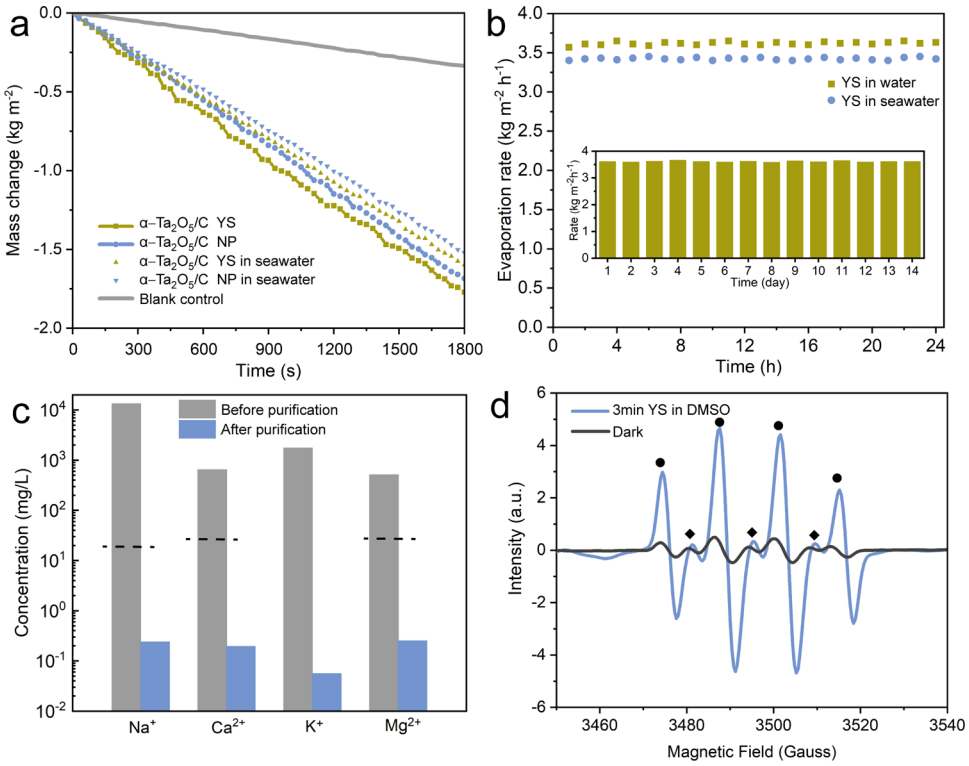

Figure 4. Water treatment performance and stability test. (a) Mass loss of water with the corresponding evaporation rate of α-Ta_2O_5/C yolk−shell and nanoparticles under 1 sun, i.e., 1 kW m^{-2}. (b) Stability test for water evaporation with various water samples for 24 h and the stability test for water evaporation in DI water for 14 days. (c) Concentration of ions in seawater before and after purification. (d) EPR spectrum of the hydroxyl radicals in dark and 3 min illumination conditions. ● Four-line peak with an intensity ratio of 1:2:2:1 represents DMPO-OH (g = 2.005). ♦ Three-line peak with an intensity ratio of 1:1:1 represents HDMPO-OH (g = 2.006). A higher intensity of DMPO-OH (●) indicates that more hydroxyl radicals are present.

imentally assessed by differential scanning calorimetry (DSC) by the sapphire referring method. Interestingly, complex hierarchical microstructures, such as the amorphous Ta_2O_5/C YS sample, have a larger heat capacity compared with Ta_2O_5/C NPs (Figure 3c). The heat capacity of amorphous Ta_2O_5/C YS is measured to be 1.85 J K^{-1} $°C^{-1}$ at 90 °C, which is 1.4 times that of nanoparticles obtained by coprecipitation (1.44 J K^{-1} $°C^{-1}$), indicating that the yolk−shell structure has the advantage of high heat storage capacity (Figure 3d). As a consequence, the external solar-thermal conversion efficiency (η_{ext}) was calculated to be 91% by fitting the temperature cooling curve for α-Ta_2O_5/C YS with an exponential function (Figure S6 and Table S3).

Furthermore, α-Ta_2O_5/C YS and α-Ta_2O_5/C NP were applied in water desalination and purification under solar irradiation. High evaporation rates of approx. 3.54 and 3.2 kg m^{-2} h^{-1} were achieved with α-Ta_2O_5/C YS in deionized (DI) water and seawater. However, α-Ta_2O_5/C prepared with nanoparticles exhibited evaporation rates of 3.36 and 3.04 kg m^{-2} h^{-1} under the same conditions, respectively (Figure 4a). In detail, all results were values after the subtraction of the blank control, which refers to the sample evaporation rate in a dark environment. The performance measurement of pure carbon spheres as controls was also conducted with the same conditions (Figure S7). More impressively, the evaporation rate can be maintained without any attenuation under continuous irradiation for 24 h (Figure 4b); furthermore, even after 2 weeks, the α-Ta_2O_5/C YS materials exhibited superstability in the water evaporation−purification performance (Figure 4b inset). From the DFT−Monte Carlo result (Figure S8 and Tables S4−S6), 1−1.5 nm medium-sized channels assigned to α-Ta_2O_5/C YS are remarkably higher than those in α-Ta_2O_5/C NP. Capillary and relative hydrophobic actions attributed to amorphous carbon can adjust the balance between the water diffusion rate and the water evaporation rate (Figure S9), which may be responsible for the rapid water evaporation rate endowed by α-Ta_2O_5/C YS.

For another aspect, we detected the quality of the collected water after purification; the concentrations of the four ions (Na^+, K^+, Ca^{2+}, and Mg^{2+}) in seawater after purification were lower than the WHO standard for drinking water,[56] which is 2 orders of magnitude better than the WHO standard (Figure 4c). Not only that, α-Ta_2O_5 has a suitable band gap to generate reactive oxygen species (ROS, such as hydroxyl radicals) under sun irradiation. Electron paramagnetic resonance (EPR) spectroscopy was performed by the DMPOX capture method to monitor hydroxyl radicals in the DMSO solution. A higher intensity of DMPO-OH indicates a high concentration of hydroxyl radicals generated under 3 min irradiation (Figure 4d), which can be considered as the mechanism for rapid inactivation in purified water.

CONCLUSIONS

In conclusion, the α-Ta_2O_5/C YS material was prepared by the low-temperature calcination method and applied to solar-driven interfacial water evaporation. We demonstrated that C heteroatoms could enhance the light-harvesting ability and reduce water diffusive resistance; moreover, heat concentration endowed by specific yolk−shell structures could optimize solar-thermal conversion. As a result, α-Ta_2O_5/C YS enabled a

https://doi.org/10.1021/acsomega.3c01858
ACS Omega 2023, 8, 29025−29032

water evaporation rate of 3.54 kg m^{-2} h^{-1} with a solar-thermal conversion efficiency of 91% under one sun irradiation. Furthermore, the evaporation rate of α-Ta_2O_5/C YS hardly abated in the 2-week test, indicating the excellent stability of the prepared samples. After purification, the ion (Na^+, K^+, Ca^{2+}, Mg^{2+}) concentrations in seawater were 2 orders of magnitude better than the drinking water WHO standard. Interestingly, the collected water could be sterilized by α-Ta_2O_5/C YS because of ROS radicals. This method exhibits great application prospects for drinkable water supply in border defense and island regions.

EXPERIMENTAL SECTION

Synthesis of a-Ta_2O_5/C YS. Freshly prepared CMSs (1 g) were dispersed in 50 mL of 0.05 M tantalum chloride/acetone solution by ultrasonication. After ultrasonic dispersion for 10 min, the resulting suspension was stirred for 2 h at 30 °C in a water bath. After vacuum filtering and washing with acetone three times, the sample was dried at 50 °C in an oven for 12 h. The microspheres were heated to 300 °C in an air environment with a heating rate of 5 °C min^{-1}, maintained at 300 °C for 90 min, and then cooled down to room temperature naturally.

Film Preparation and Testing Device. 50 mg of a-Ta_2O_5/C YS powder was dispersed in 2 mL of DI water in an ultrasonic bath. The dispersed mixture was deposited on absorbent cotton to form a 3 cm-diameter membrane. The obtained film was placed on one side of an H-shaped connector (volume = 200 mL), which was used as the water-holding device.

ASSOCIATED CONTENT

Supporting Information

The Supporting Information is available free of charge at https://pubs.acs.org/doi/10.1021/acsomega.3c01858.

XPS spectra of α-Ta_2O_5/C -YS and α-Ta_2O_5/C -NP; morphology of α- Ta_2O_5/C NP; band structure of crystalline Ta_2O_5 and α- Ta_2O_5/C; fitting of the temperature cooling stages of the α- Ta_2O_5/C YS sample; performance measurement of pure carbon spheres; DFT−Monte Carlo micropore analysis; contact angle measurements of α-Ta_2O_5/C YS; element analyses of α-Ta_2O_5 YS and α-Ta_2O_5 NP; mesopore/micropore analysis results; performance references for solar vapor generation materials with different morphologies (PDF)

AUTHOR INFORMATION

Corresponding Authors

Xuanbo Chen − *College of Power Engineering, Naval University of Engineering, Wuhan 430033, P. R. China;* orcid.org/0000-0002-2158-7598; Email: xbchen@ipe.ac.cn

Shuyong Liu − *College of Power Engineering, Naval University of Engineering, Wuhan 430033, P. R. China*; Email: lsydh@sina.com

Authors

Yingqi Zhu − *College of Power Engineering, Naval University of Engineering, Wuhan 430033, P. R. China*

Jinlin Liu − *College of Power Engineering, Naval University of Engineering, Wuhan 430033, P. R. China*

Jing Li − *College of Power Engineering, Naval University of Engineering, Wuhan 430033, P. R. China*

Complete contact information is available at: https://pubs.acs.org/10.1021/acsomega.3c01858

Notes

The authors declare no competing financial interest.

ACKNOWLEDGMENTS

This work was financially supported by the National Natural Science Foundation of China (Nos. 92163209, 21931012) and the Natural Science Foundation of Hubei province (No. 2022CFB405).

REFERENCES

(1) Lewis, N. S. Research Opportunities to Advance Solar Energy Utilization. *Science* **2016**, *351*, No. aad1920.

(2) Tao, P.; Ni, G.; Song, C.; Shang, W.; Wu, J.; Zhu, J.; Chen, G.; Deng, T. Solar-Driven Interfacial Evaporation. *Nat. Energy* **2018**, *3*, 1031−1041.

(3) Gao, M.; Zhu, L.; Peh, C.; Wei Ho, G. Solar Absorber Material And System Designs For Photothermal Water Vaporization Towards Clean Water And Energy Production. *Energy Environ. Sci.* **2019**, *12*, 841−864.

(4) Zhou, L.; Li, X.; Ni, G. W.; Zhu, S.; Zhu, J. The Revival of Thermal Utilization from the Sun: Interfacial Solar Vapor Generation. *Nat. Sci. Rev.* **2019**, *6*, 562−578.

(5) Li, X.; Xu, W.; Tang, M.; Zhou, L.; Zhu, B.; Zhu, S.; Zhu, J. Graphene Oxide-Based Efficient and Scalable Solar Desalination Under One Sun with A Confined 2D Water Path. *Proc. Natl. Acad. Sci. U.S.A.* **2016**, *113*, 13953−13958.

(6) Ghasemi, H.; Ni, G.; Marconnet, A. M.; Loomis, J.; Yerci, S.; Miljkovic, N.; Chen, G. Solar Steam Generation By Heat Localization. *Nat. Commun.* **2014**, *5*, No. 4449.

(7) Gao, M.; Connor, P. K. N.; Ho, G. W. Plasmonic Photothermal Directed Broadband Sunlight Harnessing for Seawater Catalysis and Desalination. *Energy Environ. Sci.* **2016**, *9*, 3151−3160.

(8) Zhou, L.; Tan, Y.; Wang, J.; Xu, W.; Yuan, Y.; Cai, W.; Zhu, S.; Zhu, J. 3D Self-Assembly of Aluminium Nanoparticles for Plasmon-Enhanced Solar Desalination. *Nat. Photonics* **2016**, *10*, 393−398.

(9) Zhou, L.; Tan, Y.; Ji, D.; Zhu, B.; Zhang, P.; Xu, J.; Gan, Q.; Yu, Z.; Zhu, J. Self-Assembly Of Highly Efficient, Broadband Plasmonic Absorbers For Solar Steam Generation. *Sci. Adv.* **2016**, *2*, No. e1501227.

(10) Ni, G.; Li, G.; Boriskina, S. V.; Li, H.; Yang, W.; Zhang, T.; Chen, G. Steam Generation Under One Sun Enabled By A Floating Structure with Thermal Concentration. *Nat. Energy* **2016**, *1*, No. 16126.

(11) Zhou, X.; Guo, Y.; Zhao, F.; Shi, W.; Yu, G. Topology-Controlled Hydration of Polymer Network In Hydrogels for Solar-Driven Wastewater Treatment. *Adv. Mater.* **2020**, *32*, No. 2007012.

(12) Guo, Y.; Zhou, X.; Zhao, F.; Bae, J.; Rosenberger, B.; Yu, G. Synergistic Energy Nano-Confinement and Water Activation In Hydrogels for Efficient Solar Water Desalination. *ACS Nano* **2019**, *13*, 7913−7919.

(13) Zhao, F.; Zhou, X.; Shi, Y.; Qian, X.; Alexander, M.; Zhao, X.; Mendez, S.; Yang, R.; Qu, L.; Yu, G. Highly Efficient Solar Vapour Generation Via Hierarchically Nanostructured Gels. *Nat. Nanotechnol.* **2018**, *13*, 489−495.

(14) Son, S.; Park, J.; Ju, J.; Huh, D. H.; Jun, J. H.; Lee, H.; et al. Broadband Meta-Absorber with Au/Ni Core−Shell Nanowires for Solar Vapor Generator. *Adv. Sustainable Syst.* **2021**, *5*, No. 2100185.

(15) Fan, X. F.; Mu, H. C.; Xu, Y. L.; Song, C. W.; Liu, Y. M. Silver Nanoparticles- Poly-dopamine Wax Gourd: An Antimicrobial Solar Evaporator with Enhanced Steam Generation. *Int. J. Energy Res.* **2022**, *46*, 8949−8961.

(16) Guo, Y.; Zhou, H. Y.; Yu, G. H.; et al. Molecular Engineering of Hydrogels for Rapid Water Disinfection and Sustainable Solar Vapor Generation. *Adv. Mater.* **2021**, *33*, No. 2102994.
(17) Alketbi, A. S.; Raza, A.; Sajjad, M.; Li, H. X.; AlMarzooqi, F.; Zhang, T. J. Direct Solar Vapor Generation with Micro-3D Printed Hydrogel Device. *EcoMat* **2022**, *4*, No. e12157.
(18) Zhang, P. P.; Zhao, F.; Shi, W.; Zhou, X. Y.; Yu, G. H.; et al. Super Water-Extracting Gels For Solar-Powered Volatile Organic Compounds Management in the Hydrological Cycle. *Adv. Mater.* **2022**, *34*, No. 2110548.
(19) Cai, C. Y.; Wang, Y. Q.; Wei, Z.; Fu, Y. Biomimetic 3D Membranes with MXene Hetero- Structures For Superior Solar Steam Generation, Water Treatment, And Electricity Generation. *Sol. RRL.* **2021**, *5*, No. 2100593.
(20) Ren, J. X.; Ding, Y.; Gong, J.; Qu, J.; Niu, R. Simultaneous Solar-Driven Steam And Electricity Generation By Cost-Effective, Easy Scale-Up Mno_2-Based Flexible Membranes. *Energy Environ. Mater.* **2022**, *6*, No. e12376.
(21) Tian, Y. Z.; Wang, X. Y.; Gu, Y. F.; Miao, Y.; et al. Versatile PVA/CS/CuO Aerogel With Superior Hydrophilic and Mechanical Properties towards Efficient Solar Steam Generation. *Nano Select.* **2021**, *2*, 2380−2389.
(22) Chen, X.; Li, P.; Wang, J.; et al. Multishelled CuO/Cu_2O Induced Fast Photo-Vapour Generation For Drinking Water. *Nano Res.* **2022**, *15*, 4117−4123.
(23) Ren, H.; Tang, M.; Guan, B.; Wang, K.; Yang, J.; Wang, F.; Wang, M.; Shan, J.; Chen, Z.; Wei, D.; et al. Hierarchical Graphene Foam For Efficient Omnidirectional Solar-Thermal Energy Conversion. *Adv. Mater.* **2017**, *29*, No. 1702590.
(24) Chen, X.; Yang, N. L.; Wang, D.; et al. Hierarchical Structure Regulation for Sequential Steps in Solar Vapor Generation. *EcoMat* **2023**, *5*, No. e12348.
(25) Zhang, X. Y.; Ren, L. P.; Xu, J.; Shang, B.; Liu, X.; Xu, W. L. Magnetically Driven Tunable 3d Structured Fe_3O_4 Vertical Array For High-Performance Solar Steam Generation. *Small* **2022**, *18*, No. 2105198.
(26) Zhang, H.; Li, L.; He, N.; Jiang, B.; Tang, D. W.; et al. Bioinspired Hierarchical Evaporator Via Cell Wall Engineering For Highly Efficient And Sustainable Solar Desalination. *EcoMat* **2022**, *4*, No. e12216.
(27) Guan, W. X.; Guo, Y. H.; Yu, G. H. Carbon Materials for Solar Water Evaporation and Desalination. *Small* **2021**, *17*, No. 2007176.
(28) Li, Y. M.; Shi, Y. Y.; Wang, H. W.; Liu, T. F.; Zheng, X. W.; Gao, S. M.; Lu, J. Recent Advances In Carbon-Based Materials For Solar-Driven Interfacial Photothermal Conversion Water Evaporation: Assemblies, Structures, Applications and Prospective. *Carbon Energy* **2023**, No. e331.
(29) Wang, S.; Deng, H.; Chang, H. Y.; Li, Y. Y.; et al. Co-Hydrothermal Carbonization of Cotton Stalks And MnO_2 For Direct Solar Steam Generation With High Efficiency. *Sol. RRL.* **2022**, *6*, No. 2100890.
(30) Lv, F. Y.; Miao, J.; Hu, J.; Orejon, D. 3D Solar Evaporation Enhancement By Superhydrophilic Copper foam Inverted Cone and Graphene Oxide Functionalization Synergistic Cooperation. *Small* **2023**, *19*, No. 2208137.
(31) Chao, J. B.; Lv, B. Z.; Zhao, Y. Q.; et al. Metal−Organic Framework-Derived Carbon Materials Loading on Poly-dopamine Modified Polyurethane Foam for Interfacial Solar Steam Generation And Seawater Desalination. *Energy Technol.* **2023**, *11*, No. 2201502.
(32) Wang, J.; Li, Y.; Deng, L.; Wei, N.; Weng, Y.; Dong, S.; Qi, D.; Qiu, J.; Chen, X.; Wu, T. High-Performance Photothermal Conversion of Narrow-Bandgap Ti_2O_3 Nanoparticles. *Adv. Mater.* **2017**, *29*, No. 1603730.
(33) Ding, D.; Huang, W.; Song, C.; Yan, M.; Guo, C.; Liu, S. Non Stoichiometric MoO_{3-X} Quantum Dots As a Light-Harvesting Material for Interfacial Water Evaporation. *Chem. Commun.* **2017**, *53*, 6744−6747.
(34) Sun, L.; Li, Z.; Su, R.; Wang, Y.; Li, Z.; Du, B.; Sun, Y.; Guan, P.; Besenbacher, F.; Yu, M. Phase-Transition Induced Conversion Into A Photothermal Material: Quasi-Metallic $WO_{2.9}$ Nano-Rods For Solar Water Evaporation And Anticancer Photothermal Therapy. *Angew. Chem. Int. Ed.* **2018**, *57*, 10666−10671.
(35) Canbazoglu, F. M.; Fan, B.; Kargar, A.; Vemuri, K.; Bandaru, P. R. Enhanced Solar Evaporation of Water From Porous Media, Through Capillary Mediated Forces and Surface Treatment. *AIP Adv.* **2016**, *6*, No. 085218.
(36) Lukyanov, A. V.; Sushchikh, M. M.; Baines, M. J.; Theofanous, T. G. Superfast Nonlinear Diffusion: Capillary Transport in Particulate Porous Media. *Phys. Rev. Lett.* **2012**, *109*, No. 214501.
(37) Campbell, P. Enhancement of Light Absorption from Randomizing and Geometric Textures. *J. Opt. Soc. Am. B* **1993**, *10*, No. 2410.
(38) Li, R.; Zhang, L.; Shi, L.; Wang, P. MXene Ti_3C_2: An Effective 2D Light-to-Heat Conversion Material. *ACS Nano* **2017**, *11*, 3752−3759.
(39) Zhu, L.; Gao, M.; Peh, C. K. N.; Ho, G. W. Solar-Driven Photothermal Nanostructured Materials Designs and Prerequisites for Evaporation And Catalysis Applications. *Mater. Horiz.* **2018**, *5*, 323−343.
(40) Thomas, O.; d'Heurle, F. M.; Charai, A. Reacted Amorphous Layers: Tantalum and Niobium Oxides. *Philos. Mag. B* **1988**, *58*, 529−538.
(41) Raghavan, S.; Hsin, W.; Ralph, B. D.; Porter, W. D.; Vaβen, R.; Stöver, D.; Mayo, M. J. Ta_2O_5/Nb_2O_5 And Y_2O_3 Co-Doped Zirconias for Thermal Barrier Coatings. *J. Am. Ceram. Soc.* **2004**, *87*, 431−437.
(42) Hu, T.; Li, L.; Yang, Y.; Zhang, J. A Yolk- Shell Super-Hydrophobic/ Super-hydrophilic Solar Evaporator for Efficient and Stable Desalination. *J. Mater. Chem. A* **2020**, *8*, 14736−14745.
(43) Zhang, Z.; Mao, D.; Yang, M.; Yu, R. Application of Hollow Multi Shelled Structures in Electromagnetic Wave Field. *Chem. Res. Chin. Univ.* **2021**, *42*, 1395−1406.
(44) Wang, J.; Wan, J.; Yang, N.; Li, Q.; Wang, D. Hollow Multi-Shell Structures Exercise Temporal−Spatial Ordering and Dynamic Smart Behavior. *Nat. Rev. Chem.* **2020**, *4*, 159−168.
(45) Wei, Y.; Yang, N.; Huang, K.; Wan, J.; You, F.; Yu, R.; Feng, S.; Wang, D. Steering Hollow Multishelled Structures in Photocatalysis: Optimizing Surface And Mass Transport. *Adv. Mater.* **2020**, *32*, No. 2002556.
(46) Chen, X.; Yang, N. L.; Wang, D.; et al. Highly Efficient Photothermal Conversion and Water Transport During Solar Evaporation Enabled By Amorphous Hollow Multishelled Nano-Composites. *Adv. Mater.* **2022**, *34*, No. 2107400.
(47) Zhan, S.; Chen, X. B.; Wang, D.; et al. Hollow Multishelled Structured Graphdiyne Realized Radioactive Water Safe-Discharging. *Nano Today* **2022**, *47*, No. 101626.
(48) Mao, D.; Wan, J.; Wang, J.; Wang, D. Sequential Templating Approach: A Groundbreaking Strategy to Create Hollow Multishelled Structures. *Adv. Mater.* **2018**, *31*, No. 1802874.
(49) Qi, Q.; Xu, L. K.; Du, J.; Yang, N. L.; Wang, D. Fabrication and Application of Graphdiyne-Based Heterogeneous Compositions: From The View Of Interaction. *Chem. Res. Chin. Univ.* **2021**, *37*, 1158−1175.
(50) Wang, C.; Wang, J.; Hu, W.; Wang, D. Controllable Synthesis of Hollow Multi-Shell Structured Co_3O_4 with Improved Rate Performance and Cyclic Stability for Super-Capacitors. *Chem. Res. Chin. Univ.* **2020**, *36*, 68−73.
(51) Wang, J. Y.; Yang, M.; Wang, D. Progress and Perspectives of Hollow Multishelled Structures. *Chin. J. Chem.* **2022**, *40*, 1190−1203.
(52) Wang, J. Y.; Wang, Z. M.; Mao, D.; Wang, D. The Development of Hollow Multishelled Structure: From the Innovation of Synthetic Method to the Discovery of New Characteristics. *Sci. Chin. Chem.* **2022**, *65*, 7−19.
(53) Lü, X.; Hu, Q.; Yang, W.; Bai, L.; Sheng, H.; Wang, L.; Huang, F.; Wen, J.; Miller, D. J.; Zhao, Y. Pressure-Induced Amorphization In Single-Crystal Ta_2O_5 Nanowires: A Kinetic Mechanism And Improved Electrical Conductivity. *J. Am. Chem. Soc.* **2013**, *135*, 13947−13953.

https://doi.org/10.1021/acsomega.3c01858
ACS Omega 2023, 8, 29025−29032

(54) Moors, M.; Adepalli, K. K.; Lu, Q.; Wedig, A.; Baumer, C.; Skaja, K.; Arndt, B.; Tuller, H. L.; Dittmann, R.; Waser, R.; et al. Resistive Switching Mechanisms On TaO_x And $SrRuO_3$ Thin-Film Surfaces Probed By Scanning Tunneling Microscopy. *ACS Nano* **2016**, *10*, 1481−1492.
(55) Kakazey, M.; Vlasova, M.; Go′Mez, V.; et al. Formation of Carbon Nano-Dots With Different Spin States In Mechanically Processed Mixtures Of ZnO With Carbon Nanoparticles: An Electron Paramagnetic Resonance Study. *Phys. Chem. Chem. Phys.* **2017**, *19*, 3670−3678.
(56) *Guidelines for Drinking-Water Quality*, 4th ed.; World Health Organization, 2011.

https://doi.org/10.1021/acsomega.3c01858
ACS Omega 2023, 8, 29025−29032